Research Square

Preprints are preliminary reports that have not undergone peer review.
They should not be considered conclusive, used to inform clinical practice,
or referenced by the media as validated information.

Cu-Doped ZnIn2S4 Nanowires on Ni Foam as Bifunctional Electrocatalysts for Alkaline Water Splitting

Mahdieh Khabbazianzadeh
Shahid Beheshti University
Mahboubeh Tasviri
m_tasviri@sbu.ac.ir

Shahid Beheshti University

Research Article

Keywords: Water Splitting, HER, OER, ZnIn2S4, doping, Chalcogenide

Posted Date: November 26th, 2026

DOI: https://doi.org/10.21203/rs.3.rs-11748039/v1

License: This work is licensed under a Creative Commons Attribution 4.0 International License.
Read Full License

Additional Declarations: No competing interests reported.

Cu-Doped $ZnIn_2S_4$ Nanowires on Ni Foam as Bifunctional Electrocatalysts for Alkaline Water Splitting

Mahdieh Khabbazianzadeh and Mahboubeh Tasviri[*]

Department of Physical Chemistry, Faculty of Chemistry and Petroleum Sciences, Shahid Beheshti University, Tehran, Iran.

Abstract

Zinc Indium Sulfide ($ZnIn_2S_4$), a promising catalyst composed of earth-abundant elements, has been extensively investigated for visible-light-driven photocatalytic applications. Its use as a standalone electrocatalyst for alkaline water splitting, however, has been comparatively less explored. This study challenges the application of $ZnIn_2S_4$ as an efficient electrocatalyst and enhances its performance by Cu doping for overall water splitting. Cu incorporation provides a systematic compositional route to modify its physicochemical and electrochemical properties for bifunctional water splitting. $Cu_xZn_{1-x}In_2S_4$ nanowires supported on Ni foam (NF) were synthesized via a hydrothermal method as a promising solution for efficient water splitting. The electrocatalyst was systematically characterized using XRD, XPS, FE-SEM, ICP, and EDX techniques and the electrochemical performance was evaluated through cyclic voltammetry (CV), linear sweep voltammetry (LSV), chronoamperometry, and electrochemical impedance spectroscopy (EIS). $Cu_{0.8}Zn_{0.2}In_2S_4$ catalyst, with a molar ratio of 8:2 of Cu to Zn, demonstrated superior activity among the tested samples, with overpotentials of 95 mV for HER and 270 mV for OER, along with favorable Tafel slopes and a cell voltage of 1.62 V for overall water splitting. These findings highlight $Cu_{0.8}Zn_{0.2}In_2S_4$ as a promising candidate for high-performance water-splitting applications.

KEYWORDS: Water Splitting, HER, OER, $ZnIn_2S_4$, doping, Chalcogenide.

[*] Corresponding author
Email: m_tasviri@sbu.ac.ir

1. Introduction

The rising global demand for renewable energy sources, along with the urgent need to reduce environmental pollution, has prompted significant research into alternative energy systems [1-3]. Electrochemical water splitting has emerged as a promising approach for producing clean hydrogen fuel via a simple and safe process [4-6]. This reaction comprises two half-reactions: the oxygen evolution reaction (OER) at the anode and the hydrogen evolution reaction (HER) at the cathode, requiring a minimum energy of 1.23 V (*vs.* the reversible hydrogen electrode, RHE) under standard conditions. However, practical application is limited by their high overpotentials, particularly OER, due to its complex multistep electron transfer mechanism [7, 8].

Both acidic and alkaline electrolytes offer specific advantages for water splitting, acidic media enhance proton mobility whereas alkaline environments provide greater stability for a wider variety of materials [9-11].

Still, challenges such as energy inefficiency and stability issues necessitate the development of improved electrocatalysts. Precious metals such as platinum (Pt), iridium oxide (IrO_2), and ruthenium oxide (RuO_2) exhibit exceptional catalytic performance, but their high cost and limited availability restrict their commercial use [12-14]. Consequently, significant efforts are focused on developing low-cost and effective alternatives [15, 16].

Transition metal-based materials, such as oxides, sulfides, nitrides, and phosphides, have demonstrated potential due to their numerous active sites, desirable electronic structures, and cost-effectiveness [17-19]. Specifically, transition metal sulfides (TMS) have attracted attention owing to their unique semiconducting properties, high conductivity, and considerable structural stability [20-22]. Among TMS, Zinc Indium Sulfide ($ZnIn_2S_4$) is a layered ternary metal sulfide that has received increasing attention as a promising material for energy conversion applications. Its layered structure, tunable electronic properties, and sulfur-rich surface make it an attractive platform for electrochemical reactions. In particular, the presence of sulfur sites can provide favorable sites for the interaction with reaction intermediates. At the same time, the layered structure offers opportunities for tailoring the surface and electronic properties of the material. These characteristics have led to growing interest in $ZnIn_2S_4$ and ZIS-based materials for hydrogen evolution and other energy-related reactions [23-25]. Despite these advantages, the intrinsic electrochemical activity of pristine $ZnIn_2S_4$ is still limited. One of the main challenges is the relatively inefficient charge transfer within the material, which can negatively affect the reaction kinetics [26]. In addition, the electronic structure of pristine ZIS may not provide an optimal interaction with key reaction intermediates. As a result, the adsorption and desorption of intermediates can remain energetically unfavorable, limiting the overall catalytic performance. Therefore, simply using pristine

$ZnIn_2S_4$ is generally not sufficient to achieve highly efficient electrocatalytic activity, and modification of its electronic and surface properties is required [27, 28].

Therefore, Cu substitution in $ZnIn_2S_4$ is not simply a way of introducing additional active metal sites; more importantly, it provides a means of tuning the electronic structure and surface chemistry of the ZIS framework. The resulting changes in charge distribution, metal-sulfur interactions, and adsorption characteristics can contribute to more favorable reaction energetics and faster charge-transfer kinetics. On this basis, $Cu_xZn_{1-x}In_2S_4$ can be considered a promising system in which the catalytic properties of $ZnIn_2S_4$ are tuned through controlled cation substitution. Understanding how the Cu content affects the structure, electronic properties, and electrochemical behavior is therefore important for establishing a clear relationship between Cu substitution and the resulting catalytic performance.

Cation substitution can significantly influence the material's electronic structure, defect distribution, and charge transfer behavior, making it an effective strategy for improving catalytic efficiency. In particular, substitution Zn^{2+} with Cu^{2+} in $ZnIn_2S_4$ lattice is of interest because it can introduce localized electronic states, modify charge transport pathways, and enhance the intrinsic catalytic activity [29, 30].

In this study, we investigate the effect of Cu(II) substitution at Zn(II) sites in hexagonal $ZnIn_2S_4$ ($Cu_xZn_{1-x}In_2S_4$) for electrochemical water splitting, involving HER, OER, and overall water splitting (OWS). The catalysts were synthesized via a simple, cost-effective hydrothermal method and supported on nickel foam (NF). The structure and composition of the materials were verified by XRD, FESEM, EDX, ICP-OES, and XPS analyses. Electrochemical examinations revealed that the optimized catalyst, $Cu_{0.8}Zn_{0.2}In_2S_4$/NF, presented exceptional performance with low overpotentials of 95 mV and 270 mV (at 10 mA cm^{-2}) for HER and OER, respectively, and a cell voltage of 1.62 V for OWS. Additionally, the catalyst demonstrated remarkable stability in alkaline media, illustrating its potential for practical applications.

2. Experimental

2.1. Reagents

All chemicals used in the present study are of analytical grade and were used as received. Double-distilled water (DD) from RO-LAB was used for all syntheses. Hydrochloric acid (HCl 37%) was purchased from Dr. Mojallali company, Iran. The chemical zinc Nitrate hexahydrate ($Zn(NO_3)_2.6H_2O$ 0.98%), copper(II) nitrate tetrahydrate ($Cu(NO_3)_2.3H_2O$ >99.9%) and thiourea (H_2NCSNH_2 >0.99%) were received from Merck KGaA. Indium(III) nitrate ($In(NO_3)_3.xH_2O$ >99.9%) was provided by Sigma-Aldrich. Ni foam (NF) with a purity of 99% and a thickness of 1.5 mm was acquired from Nanosized Company, Iran.

2.2. Preparation of Ni Foam Substrate

The Ni foam substrate was cut into 1×1 cm pieces and then cleaned by immersion in a 0.2 M HCl solution, followed by sonication for 15 minutes to remove surface nickel oxides. Subsequently, the foam was sequentially washed with ethanol and deionized (DI) water for 15 minutes each under sonication. Finally, the cleaned Ni foam was dried using nitrogen gas.

2.3. Synthesis of $Cu_xZn_{1-x}In_2S_4$/NF Catalysts

The synthesis of $Cu_xZn_{1-x}In_2S_4$/NF was carried out via a hydrothermal method, as depicted in Fig. 1. Stoichiometric amounts of zinc nitrate hexahydrate ($Zn(NO_3)_2·6H_2O$), copper(II) nitrate trihydrate ($Cu(NO_3)_2·3H_2O$; x = 0, 0.2, 0.3, 0.4, 0.5, 0.6, 0.7, 0.8, 1 mol), indium chloride ($InCl_3$), and thiourea (CH_4N_2S) were dissolved in 80 mL of deionized water under constant stirring for 10 minutes. The homogeneous solution was transferred into a 150 mL Teflon-lined stainless-steel autoclave, and the pre-cleaned Ni foam was placed in the solution. The autoclave was sealed and kept at 150 °C for 12 hours.

After the reaction, the Ni foam was taken out, rinsed carefully with DI water to remove residual impurities, and dried. The powders obtained during the hydrothermal synthesis were collected for further characterization. The synthesized catalysts were denoted as $C_xZ_{(1-x)}IS$, where x represents the molar fraction of Cu in the Zn/Cu cation sublattice of $Cu_xZn_{1-x}In_2S_4$. Accordingly, the samples were labeled as ZIS ($ZnIn_2S_4$), C2Z8IS ($Cu_{0.2}Zn_{0.8}In_2S_4$), C3Z7IS ($Cu_{0.3}Zn_{0.7}In_2S_4$), C4Z6IS ($Cu_{0.4}Zn_{0.6}In_2S_4$), C5Z5IS ($Cu_{0.5}Zn_{0.5}In_2S_4$), C6Z4IS ($Cu_{0.6}Zn_{0.4}In_2S_4$), C7Z3IS ($Cu_{0.7}Zn_{0.3}In_2S_4$), C8Z2IS ($Cu_{0.8}Zn_{0.2}In_2S_4$), and CIS ($CuIn_2S_4$).

2.4. Materials Characterization

Powder X-ray diffraction (XRD) patterns were recorded on a Philips X'Pert diffractometer (Cu Kα radiation, λ = 0.15406 nm). Field-emission scanning electron microscopy (FE-SEM, TESCAN MIRA3) equipped with energy-dispersive X-ray spectroscopy (EDX) was employed for morphological observation and elemental mapping. X-ray photoelectron spectroscopy (XPS) was performed on a Thermo Fisher Scientific K-Alpha+ spectrometer using monochromatic Al Kα radiation (1486.6 eV) to analyze surface composition and oxidation states. Bulk elemental composition and metal loading were determined by inductively coupled plasma optical emission spectroscopy (ICP-OES, Varian 730-ES). Fourier-transform infrared (FT-IR) spectra of materials were recorded by Bomem spectrometer and Raman spectra were obtained using a TASKAN DL-G100 spectrometer with a wavelength of 532 nm.

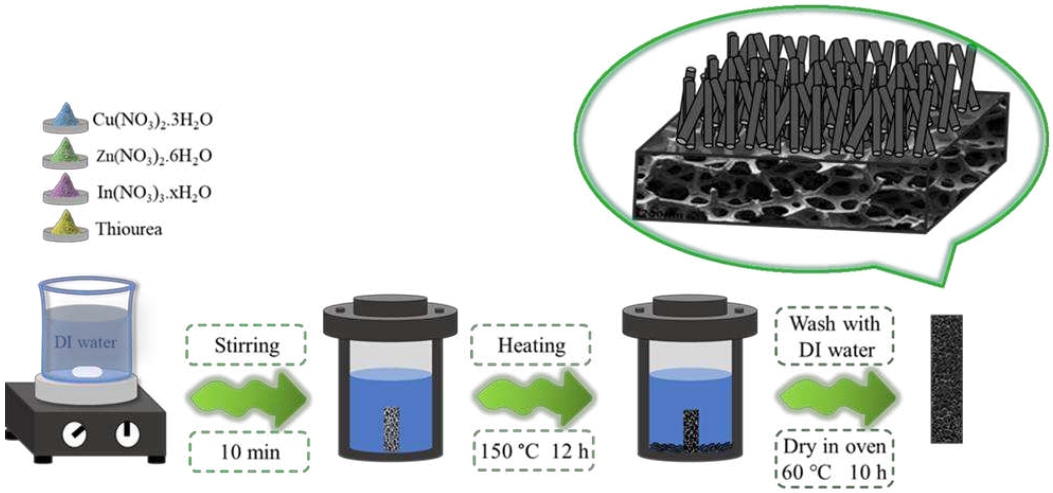


Fig. 1. Schematic illustration of the preparation of $Cu_xZn_{1-x}In_2S_4$/NF samples.

2.5. Electrochemical Measurements

Electrochemical measurements were performed on an IVIUM potentiostat (Netherlands) in a conventional three-electrode configuration, using an Ag/AgCl (3.0 M KCl) reference electrode, a Pt wire counter electrode, and catalyst-coated Ni foam as a working electrode. All experiments were carried out in a 1.0 M KOH aqueous electrolyte (pH 13.89) at ambient temperature. Prior to hydrogen evolution reaction (HER) testing, the electrolyte was purged with high-purity N_2 (99.999%) for 10 min to remove dissolved oxygen.

The electrocatalytic activities toward hydrogen evolution reaction (HER) and oxygen evolution reaction (OER) were evaluated by linear sweep voltammetry (LSV) at a scan rate of 5 mV s^{-1}. Overpotentials were determined at a current density of 10 mA cm^{-2}, and all potentials were converted to the reversible hydrogen electrode (RHE) scale.

Electrochemical impedance spectroscopy (EIS) was conducted over the frequency range of 100 kHz-0.1 Hz with a 10 mV AC perturbation. Chronoamperometric stability tests were performed at −0.10 V (HER) and 1.52 V (OER) *vs.* RHE. Prior to data acquisition, catalysts were electrochemically activated by 50 cyclic voltammetry (CV) cycles at 20 mV s^{-1}. All reported values are the average of at least three independent measurements.

3. Result and discussion

3.1 Characterization

3.1.1 X-ray diffraction pattern

The X-ray diffraction (XRD) pattern of C_8Z_2IS is presented in Fig. 2a, along with the diffraction patterns of ZIS and CIS for comparison and structural verification. The observed diffraction peaks confirm that ZIS, CIS, and C_8Z_2IS exhibit a hexagonal crystal

structure, with lattice parameters a=3.85Å and c=24.68 Å, in good agreement with the standard JCPDS data (ICDD-JCPDS card No. 01-72-0773 for $ZnIn_2S_4$) [31].

Substitution of Cu(II) for Zn(II) in the $ZnIn_2S_4$ lattice did not disrupt the hexagonal phase, as evidenced by the consistent peak positions in the samples. This indicates that the hexagonal structure of $ZnIn_2S_4$ is sufficiently robust to accommodate Cu(II) doping without significant structural distortion. This substitution is feasible due to the comparable ionic radii of Cu^{2+} (1.28 Å) and Zn^{2+} (1.38 Å), enabling homogeneous incorporation of Cu^{2+} into the $ZnIn_2S_4$ structure. The preservation of crystallinity and phase integrity after Cu substitution emphasizes the structural adaptability of $ZnIn_2S_4$ and its potential for enhanced electrocatalytic applications. The XRD patterns of the other synthesized samples are provided in the supporting information (Fig. S1). The XRD patterns of sample C_8Z_2IS before and after the electrochemical stability test were recorded and are provided in the Supporting Information (Fig. S2). As shown in Fig. S2, the characteristic diffraction peaks of the sample are well preserved after the electrochemical test, indicating the good structural stability of the catalyst under the applied electrochemical conditions.

3.1.2 Raman spectra

As shown in Fig. 2b, the Raman spectra of the three samples clearly illustrate how their vibrational behavior evolves as the composition changes from ZIS to CIS. In ZIS, the low-frequency peaks appearing around 100-200 cm^{-1} correspond to interlayer shear and bending modes, which are typical of its hexagonal layered structure. These features are clearly visible in the first spectrum, where the low-frequency region is smooth and well-defined, confirming the integrity of the layered In-S framework. The peaks observed between roughly 280 and 320 cm^{-1} arise from Zn-S and In-S bending vibrations, while the stronger features at higher frequencies, particularly in the 550-620 and 650-720 cm^{-1} regions, are attributed to Zn-S stretching and the characteristic A_1g symmetric stretching of In-S. Together, these modes form the well-established Raman fingerprint of hexagonal ZIS.

With partial substitution of Zn^{2+} by Cu^{2+} in C_8Z_2IS, the spectrum begins to shift slightly, which is evident in the second plot of the figure. Some peaks move toward lower wavenumbers and become broader, reflecting lattice softening caused by Cu incorporation. Additional weak bands appear around 260-300 cm^{-1}, corresponding to Cu-S vibrations and confirming successful Cu substitution rather than phase separation. Despite these changes, the overall spectral profile still resembles that of ZIS, consistent with a solid-solution behavior.

In CIS, the Raman pattern changes more noticeably. As seen in the third spectrum, the peaks around 150-200 cm^{-1} originate from Cu-S tetrahedral vibrations rather than interlayer modes, reflecting the Hexagonal-type structure of CIS. The absence of the strong A_1g In-S mode near 650-720 cm^{-1}, which is prominent in ZIS, clearly indicates a

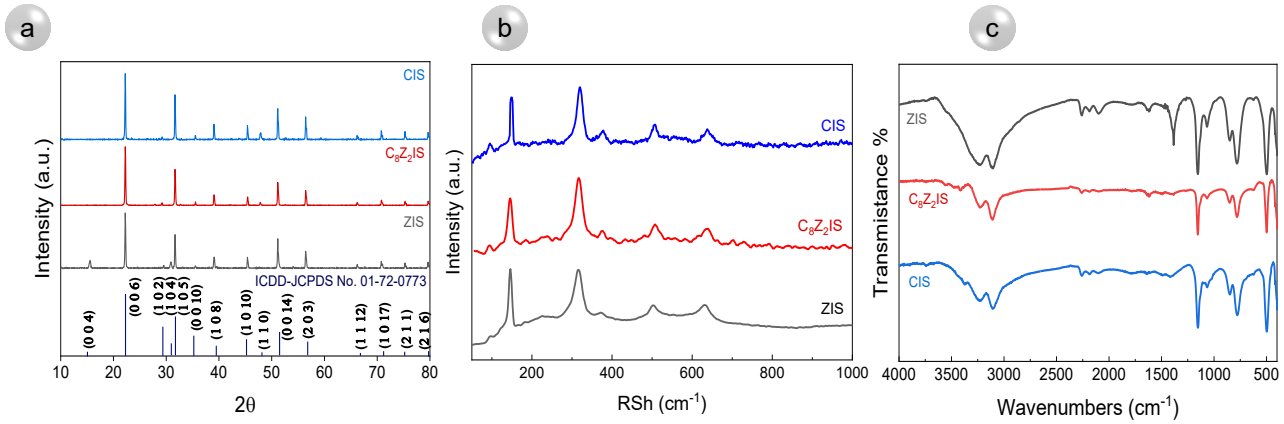


Fig. 2. a) XRD patterns, b) Raman spectra, and c) FTIR spectra of ZIS, C_8Z_2IS, and CIS.

structural difference. The redistribution of the mid-frequency vibrations further supports the formation of the CIS phase.

A small amount of surface-adsorbed water may be responsible for slightly enhancing some of the surface-related bands, particularly those in the 550-750 cm^{-1} region, or causing mild broadening of the low-frequency modes. However, these are purely surface effects and do not affect the intrinsic lattice vibrations. The main Raman features in all three samples remain consistent with their expected crystalline structures.

Overall, the peak positions, relative intensities, and overall shapes of the spectra in Fig. 2b confirm the formation of hexagonal ZIS, C_8Z_2IS, and CIS with no evidence of secondary phases.

3.1.3 FTIR

The FTIR spectra of ZIS, CIS, and C_8Z_2IS were recorded to identify the characteristic vibrational modes and to confirm the formation of metal–sulfur bonds in the synthesized materials (Fig. 2c). All samples exhibit a broad absorption band centred around 3300-3400 cm^{-1}, which is attributed to O-H stretching vibrations of physically adsorbed moisture on the surface. A weak signal in the 2900-3000 cm^{-1} range corresponds to residual C-H stretching, originating from trace organic fragments of the precursors or solvents used during synthesis. Additionally, a clear absorption band located at ~1630-1650 cm^{-1} is assigned to the bending vibration of H-O-H groups, further indicating the presence of surface-adsorbed water.

A sharp and well-defined band is observed in the region of 1200-1400 cm^{-1} for all three samples. This feature is unrelated to the intrinsic metal–sulfur vibrations and is instead attributed to the stretching modes of C-N, C-O, or symmetric COO^- groups, originating from organic residues of the precursor species. The band appears more intense in ZIS, reflecting its layered structure and higher tendency to adsorb organic moieties. In contrast, CIS shows a weaker signal due to its more stable and less adsorptive surface.

The C_8Z_2IS sample displays an intermediate intensity with slight broadening, indicating the creation of surface defects and partial retention of organic groups induced by Cu substitution.

The most significant vibrational modes appear in the fingerprint region below 1000 cm^{-1}, which directly corresponds to the formation of M-S bonds (M = Zn, Cu, In). In ZIS, two characteristic absorption peaks are detected at 630-650 cm^{-1} and ~520-540 cm^{-1}, assigned to Zn-S and In-S stretching vibrations, respectively, confirming the formation of the canonical hexagonal ZIS phase. In the case of CIS, the dominant peak is shifted to ~570-590 cm^{-1}, corresponding to Cu-S stretching, while the In-S vibration remains visible near 520-540 cm^{-1}, consistent with the chalcopyrite-like structure of CIS.

The FTIR spectrum of the doped sample C_8Z_2IS exhibits combined vibrational features of both parent phases. The simultaneous presence of the Zn–S band (~640 cm^{-1}) and the Cu-S band (~580 cm^{-1}), along with the In-S feature in the 520–540 cm^{-1} range, clearly confirms the successful incorporation of Cu into the Zn sites of the ZIS lattice. Moreover, the slight shifts and broadening of these peaks indicate lattice distortion and the generation of structural defects due to ionic radius mismatch between Zn^{2+} and Cu^{2+}. These observations collectively verify the formation of a solid-solution structure in C_8Z_2IS.

Overall, the FTIR analysis validates the formation of the intended metal–sulfur frameworks, confirms the structural identity of ZIS and CIS, and supports the presence of Cu-containing sulfur coordination environments in the C_8Z_2IS sample.

3.1.4 FE-SEM images

The morphology and size of the synthesized C_8Z_2IS catalyst were examined using field emission scanning electron microscopy (FE-SEM). FE-SEM images, as presented in Fig. 3, reveal the formation of a uniform and well-distributed array of nanowires grown directly on the Ni foam substrate. These nanowires demonstrate exceptional uniformity, with an average length of approximately 2.5 μm and a typical diameter of around 30 nm.

The nanoscale structure of the C_8Z_2IS catalyst is advantageous for enhancing its electrocatalytic efficacy, as the high aspect ratio of the nanowires offers an increased surface area and many active sites for catalytic reactions. Moreover, the uniform distribution of the nanowires throughout the conductive Ni foam substrate guarantees efficient electron transport and optimal use of the catalyst during electrochemical processes. These morphological features contribute significantly to the improved catalytic activity observed for C_8Z_2IS in water splitting applications.

Energy-dispersive X-ray spectroscopy (EDX) analysis, as shown in Fig. 4a, confirms that the synthesized nanowires consist of zinc (Zn), copper (Cu), indium (In), and sulfur (S). Molecular ratio of Zn:Cu:In:S in the nanowires, determined by EDX quantitative analysis,

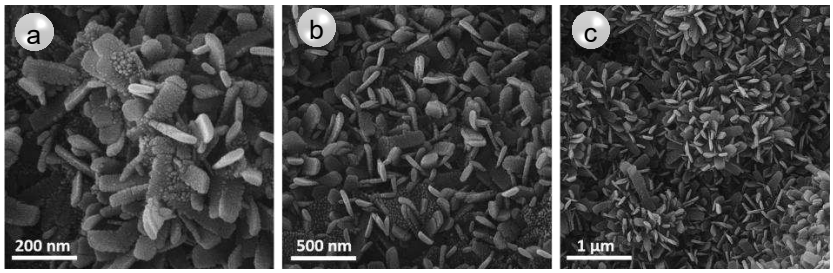


Fig. 3. FE-SEM micrograph of C_8Z_2IS with various magnifications.

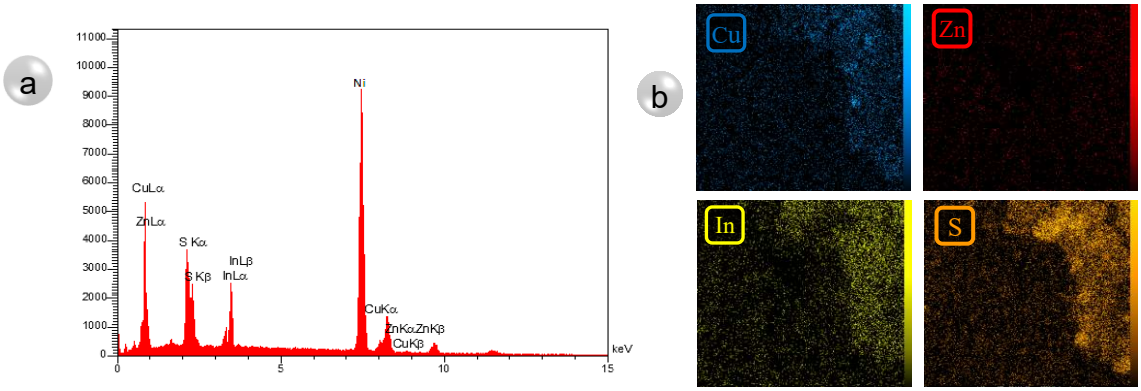


Fig. 4. a) EDX spectrum, and b) Elemental

closely matches the stoichiometric ratio of the bulk material, indicating uniform composition during the synthesis process. Furthermore, the elemental mapping images for Zn, Cu, In, and S, illustrated in Fig. 4b, demonstrate the distribution of these elements over the nanowires. The observed uniformity highlights the effectiveness of the synthesis method in attaining consistent elemental incorporation.

Moreover, inductively coupled plasma optical emission spectroscopy (ICP-OES) analysis, as summarized in Table 1, validates the accurate stoichiometric ratios of the elements, verifying the EDX results. This findings together demonstrate the successful synthesis and uniform elemental composition of the nanowires.

Table 1. Results of ICP-OES analysis of the synthesized C_8Z_2IS.

Element	***Wavelength (nm)***	***Wt.%***	***Mol***
Cu	327.395	12.0	4.14
Zn	334.502	3.0	1.00
In	410.176	54.2	10.37
S	181.972	30.8	21.07

3.1.4. X-ray photoelectron spectroscopy

X-ray photoelectron spectroscopy (XPS) was conducted to investigate the surface composition and chemical states of the synthesized C_8Z_2IS sample. Survey spectrum, as depicted in Fig. 5a, confirms the presence of zinc (Zn), copper (Cu), indium (In), and sulfur (S) as the major surface elements, as indicated by their characteristic binding energy peaks.

High-resolution XPS spectra for core levels of Zn, Cu, In, and S (Fig. 5b-e) provide detailed insights into their chemical states. The Zn-2p spectrum exhibits two distinct peaks at 1021.4 eV (Zn $2p_{3/2}$) and 1043.7 eV (Zn $2p_{1/2}$), corresponding to Zn^{2+} oxidation states. Similarly, the Cu-2p spectrum reveals peaks at 932.5 eV (Cu $2p_{3/2}$) and 952.7 eV (Cu $2p_{1/2}$), thereby verifying the Cu^{2+} oxidation state. The In-3d spectrum displays peaks at 444.8 eV (In $3d_{5/2}$) and 452.4 eV (In $3d_{3/2}$), characteristic of In^{3+} oxidation states. Finally, the S-2p spectrum exhibits peaks at 162.1 eV (S $2p_{3/2}$) and 163.8 eV (S $2p_{1/2}$), suggesting the presence of sulfide species.

The findings affirm the successful combination of Zn, Cu, In, and S in the synthesized nanostructure and validate their expected oxidation states, which are crucial for its intended electrocatalytic applications [32, 33].

The structural evolution and phase formation of the synthesized samples were comprehensively confirmed by the combined XRD, FTIR, Raman, and XPS analyses. The XRD patterns exhibited diffraction peaks that matched well with the characteristic reflections of the hexagonal crystal structure, indicating the successful formation of the desired phases without detectable impurity phases. The FTIR spectra further verified the formation of metal–sulfur bonds through the characteristic vibrational modes associated with Zn-S, Cu-S, and In-S linkages. Consistent with these findings, the Raman spectra displayed the characteristic lattice vibrational modes of the hexagonal sulfide framework, while the gradual shifts in peak positions and changes in intensity with Cu incorporation suggest possible changes in the lattice structure and local coordination environment. Furthermore, XPS analysis confirmed the presence of Zn, Cu, In, and S elements with the expected chemical states, providing additional evidence for successful incorporation of Cu into the host lattice. The excellent agreement among the XRD, FTIR, Raman, and XPS results demonstrates that Cu substitution occurred within the $ZnIn_2S_4$ framework without altering the overall hexagonal structure, leading to the successful formation of phase-pure $ZnIn_2S_4$, $Cu_{0.8}Zn_{0.2}In_2S_4$, and $CuIn_2S_4$ samples.

3.2. Electrochemical performance

Linear sweep voltammetry (LSV) measurements, illustrated in Fig. 6a, indicate that C_8Z_2IS exhibits the most favorable hydrogen evolution reaction (HER) performance, achieving a current density of 10 mA cm^{-2} with an overpotential (η) of only 95 mV at a

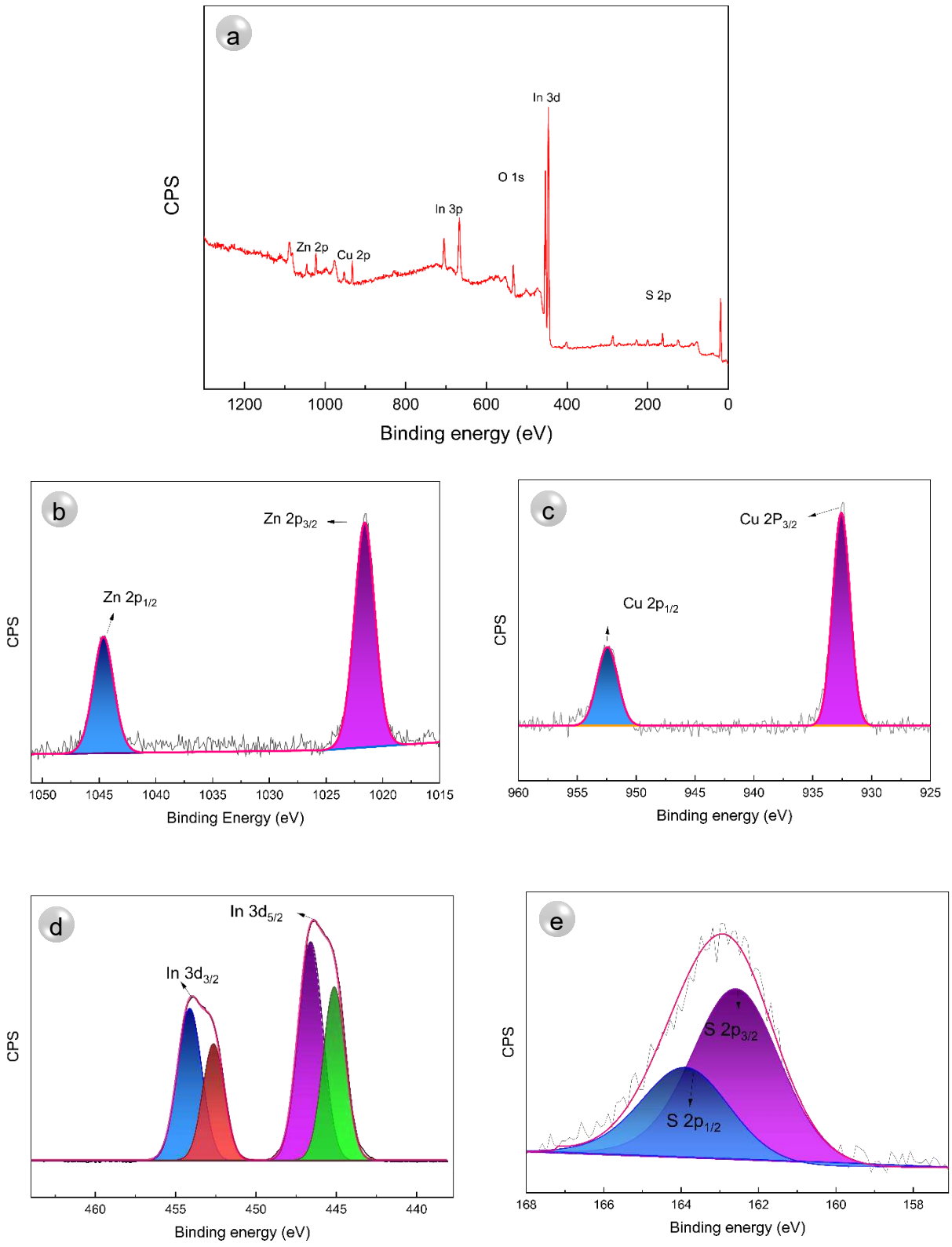


Fig. 5. XPS spectra of synthesized C_8Z_2IS: a) survey spectrum, and high-resolution spectra for (b) Zn-2p, (c) Cu-2p, (d) In-3d, and (e) S-2p micrograph of C_8Z_2IS with various magnifications.

scan rate of 5 mV s^{-1}. This demonstrates its superior activity compared to other synthesized samples. In order to further assess the electrocatalytic kinetics, Tafel plots were analyzed (Fig. 6c). C_8Z_2IS sample displayed the lowest Tafel slope of 82 mV dec^{-1} among the samples, reflecting its improved reaction kinetics and reduced energy barriers for HER.

An effective electrocatalyst for water splitting must exhibit high activity for both HER and OER, enabling efficient overall water splitting while reducing costs. The OER activity of the synthesized electrodes was examined in a similar electrochemical setup with a scan rate of 5 mV s^{-1}. As shown in Fig. 6b, C_8Z_2IS achieved the most favorable OER performance, with an overpotential of 270 mV to deliver a current density of 10 mA cm^{-2}. Furthermore, the Tafel plot for OER (Fig. 6d) indicates a Tafel slope of 45 mV dec^{-1} for C_8Z_2IS, the lowest among all synthesized electrocatalysts, emphasizing its exceptional reaction kinetics for OER. The LSV curves and corresponding Tafel plots for the other samples are presented in the supporting information (Fig. S3).

Electrochemical impedance spectroscopy (EIS) was performed to elucidate the charge transfer resistance during HER and OER. The Nyquist plots (Fig. 6e and f) illustrate that C_8Z_2IS exhibits smaller semicircle diameters compared to other samples, implying enhanced charge transfer efficiency and lower resistance. These findings match well with the superior performance observed in the LSV and Tafel analyses for both HER and OER, consequently verifying the catalytic efficiency of C_8Z_2IS. The fitted EIS parameters and corresponding equivalent circuit are presented in Table S1 and Fig. S4.

The electrochemically active surface area (ECSA) of the synthesized catalysts was evaluated by cyclic voltammetry (CV) performed in the non-faradaic potential region at various scan rates (Fig. S5 a-i). The double-layer capacitance (C_{dl}) was extracted from the slope of the linear relationship between the current density difference ($\Delta j = (j_a - j_c)/2$) and the scan rate, where a higher slope corresponds to a larger ECSA (Fig. S5 j).

As illustrated in the corresponding plot in Fig. S5 j, the C_8Z_2IS catalyst exhibits the highest C_{dl} value of 5.3 mF cm^{-2}, indicating a significantly enhanced electrochemically active surface area compared with the other samples. This result suggests that the partial substitution of Cu^{2+} for Zn^{2+} in the $ZnIn_2S_4$ lattice effectively modulates the surface charge distribution and introduces more exposed active sites, thereby promoting the adsorption and desorption of reaction intermediates during electrochemical processes.

The remarkable increase in C_{dl} implies that C_8Z_2IS possesses a rougher surface texture and a higher density of accessible catalytic sites, which facilitate faster charge transfer across the electrode–electrolyte interface. Such interfacial optimization is crucial for achieving efficient electron mobility and minimizing overpotential losses during both the hydrogen evolution reaction (HER) and the oxygen evolution reaction (OER). Consequently, the outstanding C_{dl} value of C_8Z_2IS strongly correlates with its superior

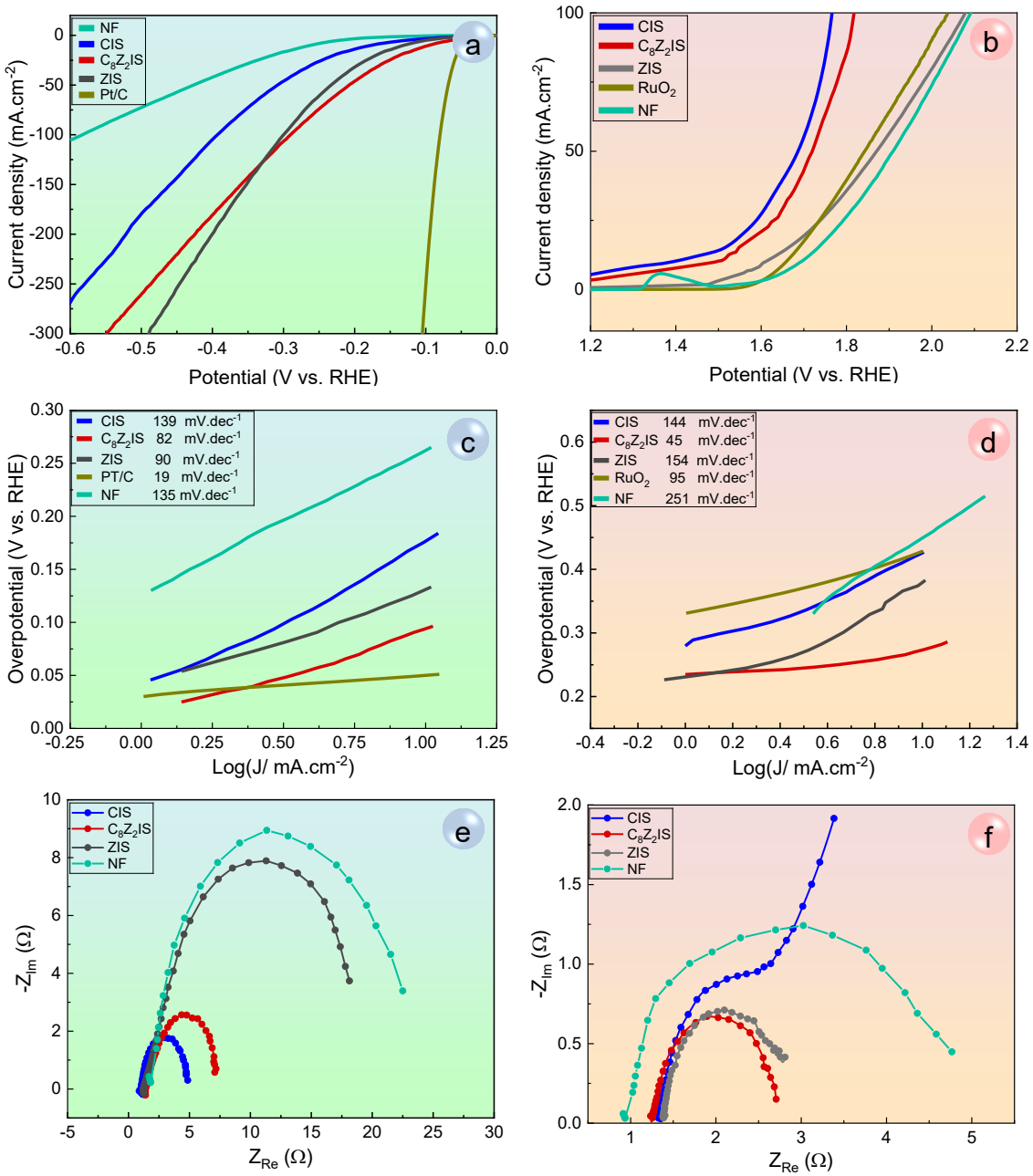


Fig. 6. HER and OER activity of the electrocatalysts in 1.0 M KOH: a) LSV curves for HER with IR correction, b) LSV curves for OER with IR correction, c) Tafel plots of all samples in 1.0 M KOH for HER, d) Tafel plot of all samples in 1.0 M KOH for OER,

overall water-splitting activity, confirming that its structural and compositional design plays a pivotal role in enhancing electrochemical performance.

The electrochemical performance of the synthesized C_8Z_2IS catalyst was evaluated for overall water splitting in a two-electrode setup. Linear sweep voltammetry (LSV) measurements were conducted in the potential range of 1.2-1.9 V, as shown in Fig. 7. In

this setup, the synthesized C_8Z_2IS was utilized as both the working and counter electrodes, and the corresponding current densities were recorded by systematically varying the applied potential.

Remarkably, the C_8Z_2IS-based electrolyzer required only 1.62 V to reach a current density of 10 mA cm^{-2}. This value is significantly lower than those reported for many recently synthesized electrocatalysts, demonstrating the outstanding efficiency of C_8Z_2IS in driving both HER and OER simultaneously. The exceptional activity of C_8Z_2IS can be attributed to its optimized composition, high electrical conductivity, and abundant active sites, which altogether promote charge transfer and catalytic performance during the overall water-splitting process.

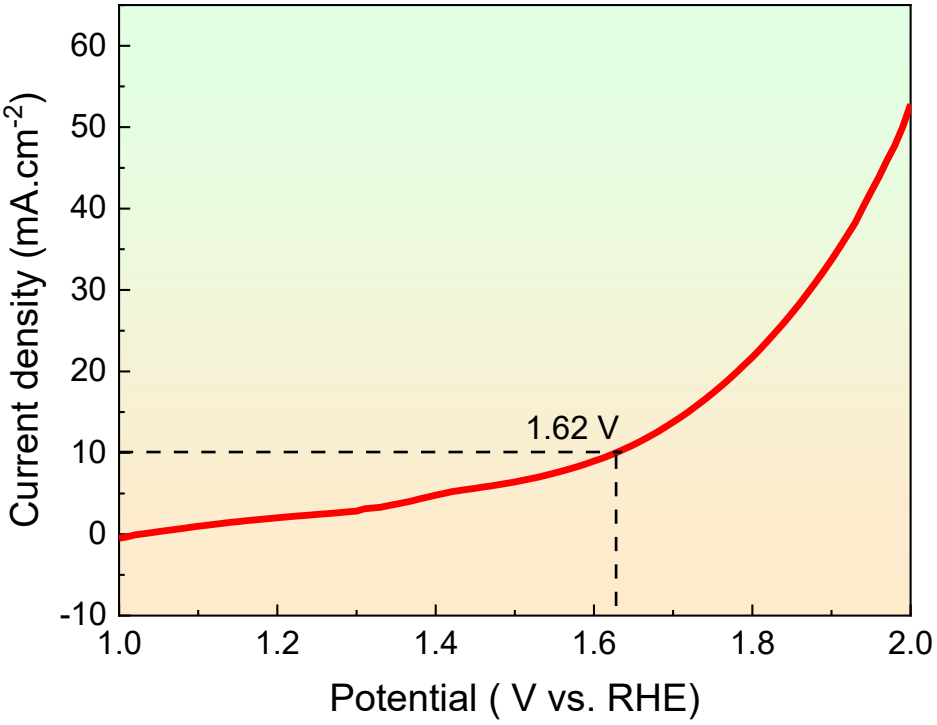


Fig. 7. LSV curve for overall water splitting, applying C_8Z_2IS as both the working and counter electrodes in 1.0 M KOH.

The stability of the C_8Z_2IS electrocatalyst for both the HER and OER was evaluated through continuous chronoamperometric response (i-t) measurements, as presented in Fig. 8a and b. The tests were performed under alkaline conditions (1.0 M KOH) at applied potentials of -0.10 and -0.23 V for HER and 1.52 and 1.75V (*vs.* RHE) for OER. The results demonstrate exceptional durability, with negligible current decay over 10 hours of continuous operation, reflecting the robust stability of the C_8Z_2IS electrocatalyst under operating conditions. For comparison, the chronoamperometric response of bare Ni foam

was recorded under identical experimental conditions, and the corresponding current-time curve is provided in the Supporting Information (Fig. S6).

Cyclic voltammetry (CV) studies were also performed to evaluate the stability of C_8Z_2IS. HER stability was examined in the potential range of -0.40 to 0.00 V, while OER stability was tested between 1.35 and 1.75 V (Fig. 8c and d). Comparison of the first and 1000th cycles demonstrates small changes in the CV profiles, emphasizing the remarkable stability of the C_8Z_2IS electrode during repeated cycling.

These findings together indicate the excellent electrochemical stability and durability of the synthesized C_8Z_2IS electrocatalyst in both HER and OER, making it a promising candidate for long-term water-splitting applications under alkaline conditions.

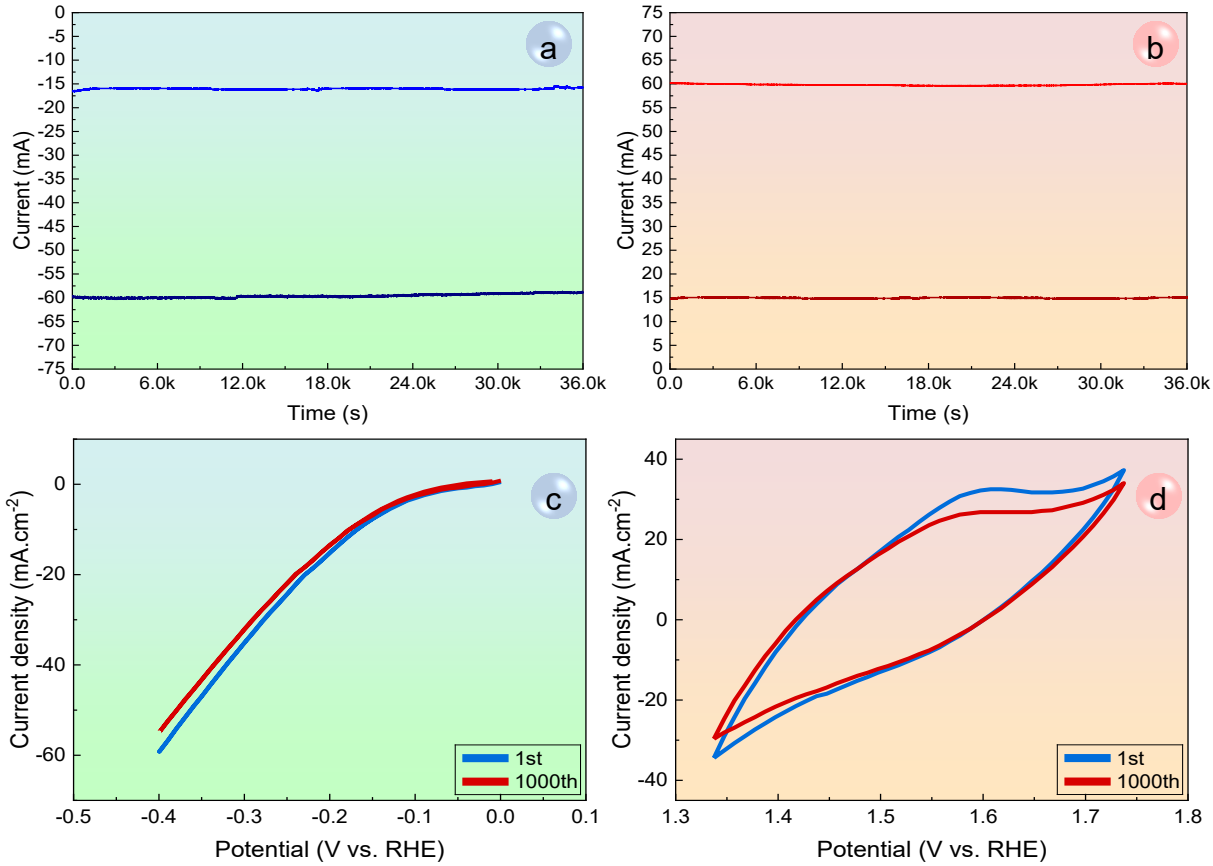


Fig. 8. Stability of the C_8Z_2IS electrocatalyst in 1.0 M KOH a) i-t plot for HER in two current densities; b) i-t plot for OER in two current densities; c) CV plot for HER; d) CV plot for OER.

Based on electrochemical investigations conducted on synthesized samples, it has been observed that compounds with higher copper content exhibit better electrochemical properties in water splitting reactions compared to zinc-containing ones. This could be attributed to certain advantages of copper over zinc and the effect of its incorporation into the sulfide structure. Copper's superior catalytic activity stems from its ability to efficiently facilitate the electrochemical reactions involved in water splitting [34]. Compared to zinc, copper has a more favorable electronic structure for catalyzing both HER and OER. This means that copper-based sulfide catalysts can achieve higher reaction rates and lower overpotentials, leading to increased efficiency in electrolysis processes. In addition, copper is an excellent conductor of electricity, which means that electrons can move more freely through copper-based sulfide catalysts compared to those containing zinc. This higher electrical conductivity enables faster electron transfer kinetics at the electrode-electrolyte interface, reducing internal resistance and energy losses during water splitting reactions. Furthermore, copper sulfides are generally more stable and durable than zinc sulfides under harsh conditions encountered during water splitting. Copper-based catalysts exhibit better resistance to corrosion and degradation, ensuring prolonged catalyst lifetime and consistent performance over time. Moreover, copper is one of the most abundant transition metals in the earth's crust and is significantly more cost-effective than zinc that make copper-based catalysts economically viable for large-scale water splitting applications [35, 36].

In conclusion, replacing zinc with copper in metal sulfides as electrocatalysts for water splitting offers numerous advantages. These attributes make copper-based sulfide catalysts promising candidates for advancing the development of sustainable hydrogen production technologies.

For a comprehensive assessment of electrocatalytic performance, the HER and OER activities of C_8Z_2IS (this work) were compared with those of several previously reported sulfide-based catalysts under identical experimental conditions (Fig. 9). In the hydrogen evolution reaction, C_8Z_2IS exhibits an exceptionally low overpotential of 95 mV, which highlights the superior intrinsic HER activity of C_8Z_2IS compared to its counterparts. For oxygen evolution reaction, C_8Z_2IS requires an overpotential of 270 mV, which is comparable to or lower than that of other catalysts, making it a favorable candidate as a bifunctional electrocatalyst [37-41].

Taken together, the outstanding HER performance combined with the competitive OER activity demonstrates that C_8Z_2IS stands out as an efficient bifunctional catalyst with great potential for practical overall water splitting applications.

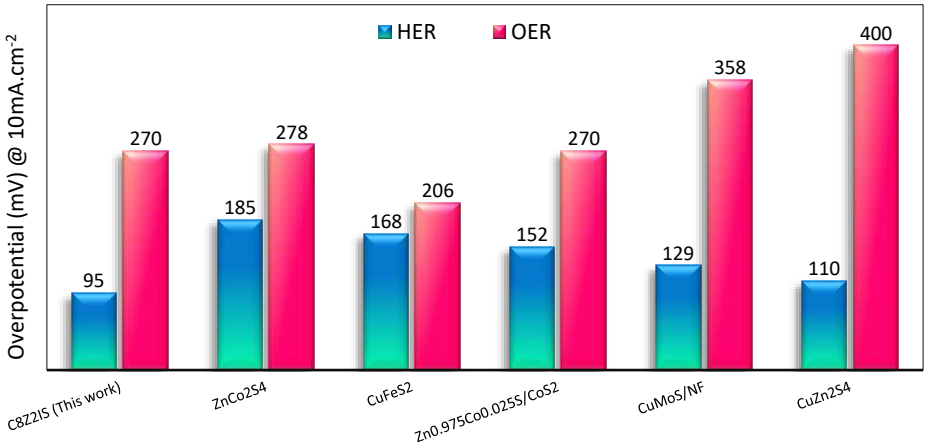


Fig. 9. Comparison of the HER and OER overpotentials for C_8Z_2IS with other reported electrocatalysts.

Proposed Mechanism

A plausible mechanism for overall water splitting over the $Cu_{0.8}Zn_{0.2}In_2S_4$/NF electrode in alkaline electrolyte can be proposed based on the involvement of Cu-modified surface active sites. During HER, the reaction is initiated by the adsorption and dissociation of water at the active sites, which can be represented by the Volmer step:

$$H_2O + e^- + * \rightarrow H^* + OH^-$$

The incorporation of Cu into the $ZnIn_2S_4$ lattice can modify the local electronic environment of the neighboring S/In sites and facilitate the activation of the H-OH bond, thereby promoting the formation of H* intermediates. The subsequent hydrogen evolution may proceed through either the Heyrovsky reaction:

$$H^* + H_2O + e^- \rightarrow H_2 + OH^- + *$$

or the Tafel reaction:

$$2H^* \rightarrow H_2 + 2*$$

For OER, hydroxide ions are initially adsorbed at the Cu-modified active sites:

$$OH^- + * \rightarrow OH^* + e^-$$

The surface OH* intermediate can then undergo further deprotonation to form O*:

$$OH^* + OH^- \rightarrow O^* + H_2O + e^-$$

Subsequently, O* reacts with another OH^- species to generate the OOH* intermediate:

$$O^* + OH^- \rightarrow OOH^* + e^-$$

Finally, OOH* is converted into molecular oxygen:

$OOH^* + OH^- \rightarrow O_2 + H_2O + e^- + *$

In this process, the Cu species incorporated into the $ZnIn_2S_4$ framework may serve as electronic modifiers of the surrounding coordination environment, facilitating the activation of H_2O for HER and tuning the adsorption strength of OH*, O*, and OOH* intermediates for OER. Therefore, the synergistic interaction between Cu and the neighboring In/S sites is proposed to regulate the adsorption and conversion of key reaction intermediates, providing a plausible pathway for the overall water-splitting process.

Conclusion

The research presented in this article highlights the potential of $Cu_xZn_{1-x}In_2S_4$ nanowires as efficient electrocatalysts for overall water splitting. Through a meticulous hydrothermal synthesis process, the catalysts demonstrated promising performance for both hydrogen and oxygen evolution reactions. The electrochemical characterization, including cyclic voltammetry, Linear sweep voltammetry, chronoamperometry and electrochemical impedance spectroscopy, provided valuable insights into the catalyst's activity and stability.

The results indicate that the $Cu_{0.8}Zn_{0.2}In_2S_4$ catalyst, with a molar ratio of 8:2 of Cu to Zn, exhibited outstanding performance, with low overpotentials of 95 mV for HER and 270 mV for OER, along with favorable Tafel slopes. The structural analysis conducted through XRD, FE-SEM, EDX, ICP-OES, and XPS confirmed the successful synthesis of the desired electrocatalyst, validating its composition and morphology. The electrochemical tests revealed that the $Cu_{0.8}Zn_{0.2}In_2S_4$ catalyst demonstrated superior activity and stability compared to other synthesized samples. The excellent performance in both HER and OER, as well as overall water splitting, underscores its potential for practical applications in renewable energy technologies.

In summary, this study contributes to the ongoing efforts in developing sustainable hydrogen production technologies by introducing a highly efficient and stable electrocatalyst for water splitting. Further research and optimization of $Cu_{0.8}Zn_{0.2}In_2S_4$ nanowires may lead to advancements in renewable energy generation and address the global challenges of energy sustainability and environmental pollution.

Acknowledgments

The authors would like to thank the Research Council of Shahid Beheshti University for its support.

Authorship contribution statement

M.K. contributed to conceptualization, methodology, investigation, formal analysis, data curation, visualization, and writing the original draft. M.T. contributed to conceptualization, supervision, writing - review and editing, and project administration. All authors reviewed and approved the final manuscript.

Declarations:

Declaration of competing interest

The authors declare that they have no known competing financial interests or personal relationships that could have appeared to influence the work reported in this paper.

Data Availability

The data supporting the findings of this study are available from the corresponding author upon reasonable request.

Funding

The authors received no financial support for the research, authorship, and/or publication of this article.

Clinical Trial Registration

Not applicable.

Ethics, Consent to Participate, and Consent to Publish

Ethics, Consent to Participate, and Consent to Publish declarations: not applicable.

Declaration of Generative AI and AI-assisted Technologies in the Writing Process

During the preparation of this work, the authors used ChatGPT (OpenAI) in order to improve the linguistic clarity, grammar, and stylistic fluency of the English text. After using this tool, the authors reviewed and edited the content as needed and took full responsibility for the content of the publication.

References

[1] Y. Li, W. Teng, H. Xu, F. Niu, Y. He, X. Zheng, S. Song, P. Tian, J. Liu, Heterostructured NiSe@NiFeCo LDH nanoflowers and NiSe@NiFeMn LDH nanoplates as electrocatalysts for efficient overall water splitting, Applied Surface Science, 740 (2026) 167016.

[2] S. Swain, B. Sirichandana, P. Bhol, K.S. Anantharaju, G. Hegde, 2D bifunctional materials: unlocking innovations for efficient water splitting, Sustainable Energy & Fuels, 9 (2025) 2870–2899.

[3] C. Moon, B. Shin, Review on light absorbing materials for unassisted photoelectrochemical water splitting and systematic classifications of device architectures, Discover Materials, 2 (2022) 5.

[4] C. Miao, X. Zheng, J. Sun, H. Wang, J. Qiao, N. Han, S. Wang, W. Gao, X. Liu, Z.-x. Yang, Facile Electrodeposition of Amorphous Nickel/Nickel Sulfide Composite Films for High-Efficiency Hydrogen Evolution Reaction, ACS Applied Energy Materials, 4 (2021) 927–933.

[5] H. Saleem, M. Khosravi, S. Maroufi, V. Sahajwalla, A.P. O'Mullane, Repurposing metal containing wastes and mass-produced materials as electrocatalysts for water electrolysis, Sustainable Energy & Fuels, 6 (2022) 4829–4844.

[6] K.P. Channabasavana Hundi Puttaningaiah, S. Aralekallu, L. Koodlur Sannegowda, Coordination organic framework of phthalocyanine with carbon nanotubes for elevating oxygen evolution reaction, Discover Materials, (2026).

[7] M. Sun, N. Zhang, Electronic Structure Engineering of Transition-Metal-based Electrocatalysts for Water Splitting, ACS Sustainable Chemistry & Engineering, 12 (2024) 15788–15811.

[8] T. Zhu, B. Wu, J. Xie, H. Yang, W. Zhang, Y. Sun, Construction of Cu2O@CoFe LDH Heterojunctions as Bifunctional Photoelectrodes for Light-Enhanced Electrochemical Water Splitting, ACS Sustainable Chemistry & Engineering, 11 (2023) 17482–17491.

[9] B. You, Y. Sun, Innovative Strategies for Electrocatalytic Water Splitting, Accounts of Chemical Research, 51 (2018) 1571–1580.

[10] Y. Jiao, Y. Zheng, M. Jaroniec, S.Z. Qiao, Design of electrocatalysts for oxygen- and hydrogen-involving energy conversion reactions, Chemical Society Reviews, 44 (2015) 2060–2086.

[11] X. Han, X. Lu, T. Wang, D. Zhao, P. Tao, W. Fan, J. Hu, H. Li, Y. He, Application of amorphous sulfides in electrocatalytic water splitting, Electrochimica Acta, 559 (2026) 148560.

[12] W. Song, M. Xu, X. Teng, Y. Niu, S. Gong, X. Liu, X. He, Z. Chen, Construction of self-supporting, hierarchically structured caterpillar-like NiCo2S4 arrays as an efficient trifunctional electrocatalyst for water and urea electrolysis, Nanoscale, 13 (2021) 1680–1688.

[13] R. Sreekumar, S. Radhakrishna Pillai, R. Raghavan Baby, S. Sukumaran Suseelamma, Morphology tuned Ni-WS2 coated stainless steel mesh as an efficient bi-functional electrocatalyst for water splitting, Materials Today Communications, 44 (2025) 111860.
[14] Z. Zhang, D. Vieira, J.E. Barralet, G. Merle, Amorphous multimetal based catalyst for oxygen evolution reaction, Discover Materials, 4 (2024) 19.
[15] S. Czioska, J. Wang, X. Teng, Z. Chen, Hierarchically Structured CuCo2S4 Nanowire Arrays as Efficient Bifunctional Electrocatalyst for Overall Water Splitting, ACS Sustainable Chemistry & Engineering, 6 (2018) 11877–11883.
[16] M.R. Prakash, M. Mathankumar, B. Subramanian, N. Rajasekaran, Electrodeposited Ni-W/BN composite as an efficient Bi-functional electrode for alkaline electrocatalytic water splitting application, Journal of Alloys and Compounds, 1083 (2026) 191614.
[17] K.C. Majhi, M. Yadav, Transition Metal-Based Chalcogenides as Electrocatalysts for Overall Water Splitting, ACS Engineering Au, 3 (2023) 278–284.
[18] Y. Liu, Y. Guo, Y. Liu, Z. Wei, K. Wang, Z. Shi, A Mini Review on Transition Metal Chalcogenides for Electrocatalytic Water Splitting: Bridging Material Design and Practical Application, Energy & Fuels, 37 (2023) 2608–2630.
[19] K. Sophanna, J. Mondal, A. Mnoyan, W.G. Shin, Controlled synthesis of Ni3S2 nanostructures on nickel foam for improved HER catalytic performance, Applied Surface Science, 718 (2026) 164771.
[20] W.-K. Chong, B.-J. Ng, L.-L. Tan, S.-P. Chai, Recent Advances in Nanoscale Engineering of Ternary Metal Sulfide-Based Heterostructures for Photocatalytic Water Splitting Applications, Energy & Fuels, 36 (2022) 4250–4267.
[21] A. Gautam, S. Sk, U. Pal, Recent advances in solution assisted synthesis of transition metal chalcogenides for photo-electrocatalytic hydrogen evolution, Physical Chemistry Chemical Physics, 24 (2022) 20638–20673.
[22] B. Fan, Z. Chen, Q. Liu, Z. Zhang, X. Fang, One-pot hydrothermal synthesis of Ni-doped ZnIn2S4 nanostructured film photoelectrodes with enhanced photoelectrochemical performance, Applied Surface Science, 370 (2016) 252–259.
[23] F. Ye, W. Liu, C. Han, Y. Zhao, P. Liu, H. Wang, Effective Anchoring of Au Nanoparticles Boosts ZnIn2S4 Photoelectrochemical Water Splitting, Crystal Growth & Design, 25 (2025) 101–108.
[24] D. Kong, H. Fan, D. Yin, D. Zhang, X. Pu, S. Yao, C. Su, AgFeO2 Nanoparticle/ZnIn2S4 Microsphere p–n Heterojunctions with Hierarchical Nanostructures for Efficient Visible-Light-Driven H2 Evolution, ACS Sustainable Chemistry & Engineering, 9 (2021) 2673–2683.
[25] J. Yao, Y. Meng, Y. He, Y. Zhao, S. Xin, F. Zhang, S. Li, Microstructure and interfacial charge regulation of flower-like In2S3/ZnIn2S4 S-scheme heterojunctions toward efficient two-electron oxygen reduction for H2O2 production, Journal of Alloys and Compounds, 1080 (2026) 190472.

[26] Q. Liu, H. Lu, Z. Shi, F. Wu, J. Guo, K. Deng, L. Li, 2D ZnIn2S4 Nanosheet/1D TiO2 Nanorod Heterostructure Arrays for Improved Photoelectrochemical Water Splitting, ACS Applied Materials & Interfaces, 6 (2014) 17200–17207.
[27] Z. Li, X. Wang, W. Tian, A. Meng, L. Yang, CoNi Bimetal Cocatalyst Modifying a Hierarchical ZnIn2S4 Nanosheet-Based Microsphere Noble-Metal-Free Photocatalyst for Efficient Visible-Light-Driven Photocatalytic Hydrogen Production, ACS Sustainable Chemistry & Engineering, 7 (2019) 20190–20201.
[28] J. Wang, S. Sun, R. Zhou, Y. Li, Z. He, H. Ding, D. Chen, W. Ao, A review: Synthesis, modification and photocatalytic applications of ZnIn2S4, Journal of Materials Science & Technology, 78 (2021) 1–19.
[29] P. Priyadarshini, P. Rout, S. Supriya, P.C. Kumar, R. Naik, Effect of Cu Concentration on Optimizing the Optical, Morphological, and Structural Characteristics of ZnIn2S4 Nanosheets for Photoresponse Applications, ACS Applied Nano Materials, 7 (2024) 28131–28144.
[30] T. Zhang, A. Yan, S. Luo, F. Huang, J. Zhang, Y. Gao, W. Zhao, Z. Liu, X. Zhao, Cu-Doped ZnIn2S4/NixP Composites with Enhanced Carrier Dynamics and Photocatalytic Hydrogen Production Performance, ACS Applied Energy Materials, 6 (2023) 1650–1660.
[31] W. Kang, F. Guo, L. Mao, Y. Liu, C. Han, L. Yuan, Ni(OH)2 surface-modified hierarchical ZnIn2S4 nanosheets: dual photocatalytic application and mechanistic insights, Physical Chemistry Chemical Physics, 25 (2023) 33175–33183.
[32] Y. Wang, D. Chen, L. Qin, J. Liang, Y. Huang, Hydrogenated ZnIn2S4 microspheres: boosting photocatalytic hydrogen evolution by sulfur vacancy engineering and mechanism insight, Physical Chemistry Chemical Physics, 21 (2019) 25484–25494.
[33] Y. Wang, J. Li, S. Chen, Y. Xie, Y. Ma, Y. Luo, Y. Ling, J. Ye, CdS/ZnIn2S4 type II heterojunctions improve photocatalytic hydrogen production: faster electron–hole separation and wider visible light utilization, Sustainable Energy & Fuels, 6 (2022) 4893–4902.
[34] J. Gautam, S.-Y. Lee, S.-J. Park, Copper-doped zinc cobalt sulfide nanosheets as advanced bifunctional electrocatalysts for sustainable hydrogen production via electrochemical water splitting, Advanced Composites and Hybrid Materials, 7 (2024) 155.
[35] Y. Wang, H. Ping, T. Tan, W. Wang, P. Ma, H. Xie, Enhanced hydrogen evolution from water splitting based on ZnO nanosheet/CdS nanoparticle heterostructures, RSC Advances, 9 (2019) 28165–28170.
[36] A.S. Sabir, E. Pervaiz, R. Khosa, U. Sohail, An inclusive review and perspective on Cu-based materials for electrochemical water splitting, RSC Advances, 13 (2023) 4963–4993.
[37] G. Song, Z. Wang, J. Sun, J. Sun, D. Yuan, L. Zhang, ZnCo2S4 nanosheet array anchored on nickel foam as electrocatalyst for electrochemical water splitting, Electrochemistry Communications, 105 (2019) 106487.

[38] Z. Yu, Y. Bai, S. Zhang, Y. Liu, N. Zhang, K. Sun, Metal–organic framework-derived Zn0.975Co0.025S/CoS2 embedded in N,S-codoped carbon nanotube/nanopolyhedra as an efficient electrocatalyst for overall water splitting, Journal of Materials Chemistry A, 6 (2018) 10441–10446.
[39] S. Nouseen, P. Singh, S. Lavate, J. Chattopadhyay, A.M. Kuchkaev, D.G. Yakhvarov, R. Srivastava, Transition metal based ternary hierarchical metal sulphide microspheres as electrocatalyst for splitting of water into hydrogen and oxygen fuel, Catalysis Today, 397-399 (2022) 618–630.
[40] N. Javed, I.A. Khan, A. Farid, K. Aftab, Transition metal sulfide electrocatalysts for water Splitting: Bridging computational design and experimental advancements, Journal of Power Sources, 656 (2025) 238057.
[41] S. Swathi, R. Yuvakkumar, G. Ravi, M. Thambidurai, H.D. Nguyen, D. Velauthapillai, Ternary Copper Iron Sulfide Microflowers Anchored on Reduced Graphene Oxide for Water Splitting, ACS Applied Nano Materials, 6 (2023) 6538–6549.

Supplementary Files

This is a list of supplementary files associated with this preprint. Click to download.

- Supplementarymaterials.docx